Brick and Block Masonry – Trends, Innovations and Challenges – Modena, da Porto & Valluzzi (Eds)
© 2016 Taylor & Francis Group, London, ISBN 978-1-138-02999-6

Experimental and numerical analyses of a masonry arch under base impulse excitation

A. Gaetani, G. Monti & M. Moroni
Sapienza University of Rome, Italy

P.B. Lourenço
University of Minho, Guimarães, Portugal

ABSTRACT: Considering the long-lasting history of the masonry arch theory, the investigation of its dynamic behavior is a relatively recent issue, which is mostly focused on the analytical formulation of the SDOF four-link rigid block mechanism. With the aim of better understanding the seismic response of vaulted masonry structures, the present study is focused on the performance of a scaled arch assembled by dry-joint 3D printed voussoirs. Due to the susceptibility of rigid bodies to base impulse excitation, the tests accounted for a set of windowed sine impulses that allowed computing a failure curve in the frequency-amplitude domain. In order to track the in-plane motion of selected points, a feature tracking based measuring technique was employed. The results have been compared with a finite element model with voussoirs assumed infinitely rigid and friction interface elements, showing an appreciable match. Eventually, the outcomes of impulse base motion tests available in literature were examined, highlighting the differences in terms of failure mechanisms and seismic capacity.

1 INTRODUCTION

In the last five decades, starting with the seminal work by Housner (1963), great effort has been devoted to the study of the rigid block dynamics, either isolated or assembled. However, despite the high seismic vulnerability of masonry vaulted structures, it is only in the 1990s that Oppenheim (1992) undertook the study of the rocking masonry arch. This was considered as a rigid body four-link SDOF mechanism in which the location of the four hinges was fixed and defined by a static equivalent analysis. The study of Oppenheim (1992) mainly focused on the capacity of the arch to recover once the mechanism is activated, that is, to go back to the rest position, without considering any post-impact behavior. In this regard, a valuable contribution was provided by Clemente (1998) who performed numerical analyses on the dynamics of stone arches under three different cases, namely free vibrations following an initial displacement, rectangular pulse and sinusoidal base acceleration. Even in this case, the author did not address the problem of the impact occurrence.

More recently, using Discrete Element Method (DEM) analyses of arches undergoing base impulse excitation, DeJong & Ochsendorf (2006) found that the approach of the cited works was not on the safe side. Only relatively large impulses cause the arch to collapse without recovering, whereas the most critical failure mode develops for smaller impulses in the post-impact phase. This behavior parallels the outcomes of Zhang & Makris (2001) for a free-standing rocking block, respectively Mode 1 and Mode 2 failure. These authors proved also that the rocking blocks are more susceptible to a one-sine than a one-cosine impulse.

Following the Oppenheim's contribution, De Lorenzis et al. (2007) proposed an analytical model able to consider the energy dissipation during the impact, thus to approximately catch the dynamic behavior of the arch in the complete cycle of rocking. Again, the arch was modelled as a four-link SDOF mechanism where the location of the hinges was assumed coincident with the one provided by a static analysis. In case of impact occurrence, the hinge location simply reflected about the vertical line of symmetry of the undeformed arch. The rocking behavior was assumed to continue back and forth producing several impacts until failure occurs or the arch returns to the rest position.

The impact problem was solved thanks to the coefficient of restitution, which relates the rotational velocity (and analogously the kinetic energy) pre- and post-impact. Conservation of angular and linear momentum (5 equations total) were used to solve for the unknowns of the problem. Although the model provided good results compared

with DEM analyses and laboratory experiments (DeJong & Ochsendorf 2006; DeJong et al. 2008), there are clearly some limitations. The strongest one regards the assumption of fixed hinge locations, which prevent the free hinge formation before and after the impact, that is, the rotation at any non-hinged joint. Moreover, sliding between blocks is neglected.

The same research group (DeJong et al. 2008) extended the previous work by means of a shaking table tests on a scaled dry-joint autoclaved aerated concrete arch. The tests regarded five time histories of real earthquakes, as well as harmonic signals and tilting analysis. Considering a one-cycle sine impulse excitation, the authors determined a simple equation fitted on the results of the analytical model. The equation describes the failure curve in terms of frequency and impulse amplitude, providing a good estimation of the stability of the arches.

In order to give more insight into the capacity of the arch under base impulse excitation, the present paper deals with the performance of a scaled arch assembled by dry-joint 3D printed voussoirs subjected to a windowed sine impulse. Moreover, a feature tracking based measuring technique was employed to monitor the in-plane displacement history of selected points on each voussoir. This provided valuable information for validating the Finite Element numerical Model (FEM) based on Coulomb friction interfaces and assumed rigid-infinitely resistant voussoirs.

The tests have been carried out in the Structures and Materials Laboratory in Sapienza University of Rome. The image analysis technique was developed at the Hydraulics Laboratory of Sapienza University of Rome.

2 EXPERIMENTAL SETUP

2.1 *Overall description*

The geometrical dimensions of the tested arch were chosen to comply with the table features, leading to a specimen of 21 voussoirs with an internal radius of 365 mm, 40 mm thick, 92 mm wide and an angle of embrace of 140° (Figure 1). The inclined supports of the arch were realized with steel angle bars bolted to the platform.

The tests were performed using an electrical-dynamic shaker with V-shaped guide rail with magnesium slip table 700×700 mm^2 large and 45 mm thick. Other specifications are reported in Table 1. The base motion was recorded using two types of ceramic shear accelerometers: a) 1034 mV/g, 0.5 to 2000 Hz, range ±5 g, accuracy 5 µg and b) 102.8 mV/g, 0.5 to 10000 Hz, range ±50 g, accuracy 150 µg.

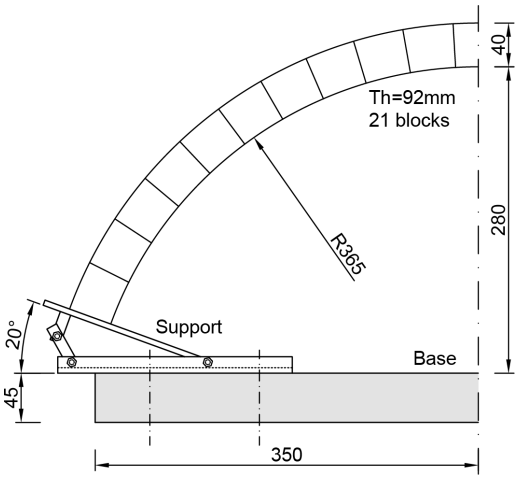

Figure 1. Tested arch geometrical dimensions.

The individual voussoirs have been printed with a 3D printer based on the Fused Deposition Modelling (FDM) technology with up to 0.1 mm accuracy. The material adopted was the Acrylonitrile Butadiene Styrene (ABS) which is a widely used thermoplastic material. Once printed, in order to reach a friction coefficient comparable with masonry elements, each voussoir has been coated with a mixture of fine sand (0.2–1.0 mm diameter grain size) and polyester bi-component resin reaching an average friction angle equal to 34.2°. The mixture bonds well to the plastic surface without showing significant deterioration along the test campaign. The same treatment was applied also to the supports in order to maintain a consistent friction angle.

Since the material properties, namely mass density, elasticity, strength, etc., do not affect the problem (Liberatore & Spera 2001; De Lorenzis et al. 2007; DeJong et al. 2008), only the external frame of the voussoirs was printed, that is, the lateral surfaces, filling the inner part with spruce wood inserts. Considering the low density of the thermoplastic material, which could compromise the stability of the model under accidental actions, the wooden inserts allowed reaching an overall mass density of around 450 kg/m^3. The total mass of the specimen was thus 1.4 kg, whereas the steel supports weight 1.7 kg each.

2.2 *Data acquisition*

According to Figure 2, reference data were provided by an acquisition system consisting of 1) a high-speed, high-resolution camera (Mikrotron EoSens) equipped with a 50-mm focal length lens capturing gray-scale images at up to 500 fps with

a resolution of 1280 × 1024 pixels (for the present set of measurements, images were acquired at 400 fps) and 2) a high-speed Camera Link digital video recorder operating in Full configuration (IO Industries DVR Express Core) to manage data acquisition and storage. The captured images were transferred to a personal computer under the control of the Express Core software. The images acquired by the Mikrotron EoSens camera have been processed using a Lagrangian Particle Tracking technique named Hybrid Lagrangian Particle Tracking (HLPT) (Shindler et al. 2012). HLPT selects image features (image portions suitable to be tracked because their luminosity remains almost unchanged for small time intervals) and tracks these from frame to frame. Though HLPT was developed to process images from fluid mechanics experiments (Moroni & Cenedese 2015), it was successfully employed here to track the texture of objects undergoing the oscillatory motion. The cornerstone of the image analysis algorithm is the solution of the Optical Flow (OF) equation, which defines the conservation of the pixel brightness intensity at time t. Since the OF equation is insufficient to compute the two unknown in-plane velocity components (i.e. the features) associated to a single pixel, the equation is computed in a window W = H × V (where H and V are the horizontal and vertical dimensions of the window respectively) centered at the pixel location. The OF equation is solved for a limited number of image pixels. The matching measure used to follow a feature (and its interrogation window) and its "most similar" region at the successive time is the "Sum of Squared Differences" (SSD) among intensity values: the displacement is defined as the one that minimizes the SSD (Moroni & Cenedese 2005). Once the trajectories are reconstructed, displacements, velocities, and accelerations are computed via central differences, which are second-order accurate.

3 EXPERIMENTAL TESTS

The first phase of the experimental campaign focused on the tilting test, i.e. quasi-static rotation of the base platform until failure occurs. Dealing with rigid blocks, a tilting test can be regarded as a first-order seismic assessment method to evaluate the collapse mechanism and the corresponding horizontal load multiplier. This is the fraction of the gravity acceleration necessary to transform the arch in a SDOF (four-link rigid block mechanism). On the other hand, being based on a quasi-static method, it assumes an infinite duration of the loading and the consequent arch stability assessment may be excessively conservative. The structure, in fact, might experience larger peaks of acceleration for short period and recover soon after (Clemente 1998; DeJong 2009).

Finally, it must be stressed that, in the local reference, tilting the model implies that the vertical acceleration reduces in magnitude as the horizontal acceleration increases. However, since the problem is pure ly based on the stability and not on the stresses within the structure, this is a non-issue. The goal is thus only the ratio between horizontal and vertical acceleration which is basically the tangent of the angle of tilt.

In order to account for possible imperfections due to the manual assembling, the test was performed three times providing an average horizontal load multiplier $\lambda = 0.29$.

Table 1. Slip table system specifications.

Shock force	12 kN
Usable frequency	5–2000 Hz
Maximum bare table acceleration	1000 m/s^2
Maximum velocity	2 m/s
Maximum displacement (peak-peak)	51 mm
Maximum load for vertical	300 kg
Effective moving mass	58 kg
Effective nominal armature mass	6 kg

3.1 *Signal processing*

As input for the shaking table tests, a sine shaped pulse was adopted. The signal needed to be processed in order to meet the features of the shaking table, which is based on an electrical-dynamic vibration system. The system is essentially based on a vibration control system that, through an amplifier, sends a signal to the shaking table where the armature moves back and forth in a magnetic

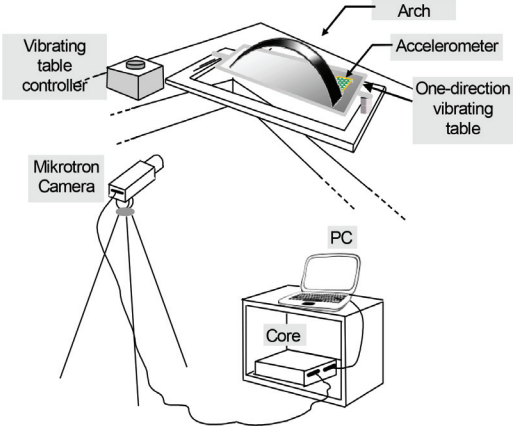

Figure 2. Experimental setup.

field. Accordingly, the acceleration (thus the displacement) of the table is governed by the amount of electric current and it was not possible to have a residual current at the end of the test, i.e. no residual displacement

In order to guarantee null displacement and velocity at the end of the test, a Bohman window was chosen to fade-in and -out the signal. Moreover, since the windowing affects the initial and final part of the signal, three cycles of sine were implemented, ensuring thus a unique central impulse.

As an example, considering a 1.3 g, and a 10 Hz three-cycle sine signal, the effects of the windowing are reported in Figure 3. As it is possible to see, the un-windowed acceleration produces a conspicuously large residual displacement (for the sake of clarity it is stopped at the end of the first cycle). On the other hand, the two accelerations are comparable in the central part of the signal.

3.2 *Experimental results*

The experimental campaign was aimed at determining the failure curve in the frequency-amplitude domain for the given shape of the impulse signal. The curve is an interpolation of the failure inputs, but, by extension, it may indicate the threshold for the stability condition: the area below the curve indicates the safe input for the arch, whereas the area over the curve indicates collapse input. In order to accomplish this goal, once the frequency was assigned, the amplitude was scaled until at least two collapses were registered. In fact, given the possible assembling imperfections, each test was repeated three times (runs).

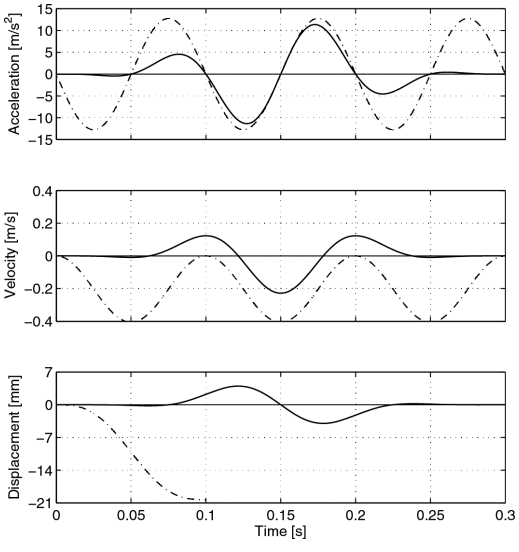

Figure 3. 1.3 g, 10 Hz pre-and post-windowed signal (dash-dot and solid line, respectively).

In general, the arch failed after the end of the input signal without experiencing any sliding between the blocks (due to the slenderness of the arch). Rocking motion occurred through apparent chaotic alternating four-hinge mechanisms, as shown in Figure 4. Conversely to the case of one-cycle sine impulse (De Lorenzis et al. 2007), additional hinges occurred when a clear four-hinge mechanism was interrupted by further impulses out-of-phase with the rocking motion (DeJong et al. 2008). Moreover, Clemente (1998) found that the arch can even (temporarily) experience larger and unsafe rotations if the subsequent impulse restores the displacements in a safety range. In general, these aspects have a stabilizing effect (larger amount of impacts leads to larger dissipated energy) and higher amplitude signals are usually necessary to bring the arch to collapse.

Focusing on the collapse trials (runs with failure), a certain trend in the behavior of the arch was detected. Considering, for instance, the time history reported in Figure 3, the first and last cycle (up to 0.1 s and after 0.2 s) did not modify the arch configuration. In fact, even in the cases the amplitude was larger than the minimum acceleration that induces the rocking motion (i.e. the value provided by tilting test, 0.29 g), the sudden change of direction did not allow any clear hinge activation.

In terms of displacement diagram, the central part of the time history resembles a one-cycle sine. This means that there are three clear base movements (phases): a) onward (from rest position to the positive peak), b) backward (until the negative peak, and represents the prominent phase) and c) again onward (until the rest position).

According to the visual inspection of the recordings inherent the arch collapses, during the phase a) the arch underwent a rigid translation without a clear formation of a mechanism. During phase b) the arch developed the usual four-hinge mechanism, whose hinge location approximately matched those indicated by the tilting test discussed before (Figure 4). Eventually, phase c), completely out-of-phase, led to a more chaotic behavior, with even a temporary occurrence of a fifth hinge.

According to the previous description, several features were persistent in most tests. In particular, considering the labels reported in Figure 4, the hinges C and D kept opening until the failure occurrence, without significant location changes. Conversely to the case of one-cycle sine impulse, for which Mode 2 can be regarded as the most critical one (Zhang & Makris 2001; DeJong & Ochsendorf 2006), in this case the failure seemed to occur without any flipping impact of these hinges. Moreover, the location of the hinges A and B showed a clear

movement: after the initial location (end of phase b), they started to migrate according to the arrows depicted in the same figure.

A total of 69 runs was performed and the results are collected in Figure 5. In order to highlight the trend of the experimental results, a linear regression analysis has been implemented (red dot line). By means of a logarithmic transformation of the data, an exponential curve constrained to asymptotically reach (for lower frequencies) the value provided by the tilting test was obtained. As it is possible to observe, the fitted line matches well the results, with a coefficient of determination equal to $R^2 = 0.98$. The result is reported in Equation 1, where f_p and a_p represent the frequency and impulse amplitude, respectively.

$$a_p = 0.0647e^{0.2801 f_p} + 0.225 \quad (1)$$

The results of the experimental campaign were compared with the curve computed according to DeJong et al. (2008, Table 3, with $\lambda = 0.30$, $C_1 = 0.02$, $C_2 = -0.81$, and $t_{min} = 0.11$). This curve represents the governing Mode 2 failure domain for a one-cycle sine impulse for the arch with 10% reduction thickness (as discussed below). Given the different input adopted, the curve is considerably more conservative. As already stressed, the reason lies in the out-of-phase acceleration that allowed the arch to experience larger peaks of acceleration without failing.

The outcome of the tilting analysis (0.29 g) is also reported in Figure 5. Since the quasi-statical nature of the test, this represents the expected asymptote (lower frequency range) of any dynamic test campaign. By extension, the horizontal load multiplier provided by the tilting test denotes the threshold of the region where impulses cause no hinge to form, i.e. the arch acts as a rigid body following the base motion. In general, the comparison between dynamic and tilting test highlights how much a quasi-statical analysis may underestimate the capacity of the arch.

Finally, it must be stressed that the elastic resonant frequency of the first mode was not evaluated. The results, in fact, are not affected by it (as for the case of elastic structures) because the natural frequency of rigid blocks changes with the displacement and the initial hinge formation immediately modifies the resonant frequency. At the most, resonance might force hinges to occur at a lower acceleration than expected (DeJong et al. 2008).

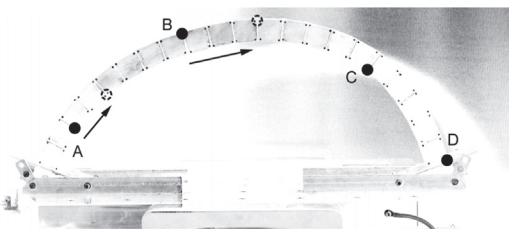

Figure 4. 7 Hz and 0.6 g impulse (first replicate): deformed shape at 0.17 s and hinge location.

4 NUMERICAL ANALYSES

4.1 *Pushover analysis*

First, it must be noted that slight variations in block size, rounded corners and the imperfection of the manually assembled geometry, may lead to a not accurate match of the voussoir lateral surfaces or a not perfect semi-circular shape, ending up with an overall reduction of stability. According to DeJong et al. (2008), this aspect was considered in the present model with an overall reduction of thickness of 10%.

Regarding the numerical analyses, a commercial FEM software, has been adopted. According to the goal of the tilting test, which is the horizontal load multiplier and the onset mechanism detection, a static nonlinear analysis (pushover) has been performed. In particular, regarding the mechanical parameters of the Coulomb friction interface, a brittle behavior was implemented with cohesion, tensile strength and dilatancy set to zero. Capital importance is assigned to the normal and tangential stiffness, discussed below. On the other hand, mass density and friction angle were equal to 450 kg/m^3 and 34°, respectively, whereas the voussoirs were assumed rigid-infinitely resistant.

The mesh was generated considering tetrahedral (TE12 L) for the voussoirs and plane triangle elements (T18IF) for the interfaces. Attention was paid to the geometrical nonlinearities and interface stiffness. Regarding the former, a Total Lagrange (TL) and an Updated Lagrange (UL) description can be used in the software, where the choice basically regards the reference configuration used to determine the stress and strain measures. In TL formulation the initial configuration is used as reference, whereas in UL formulations, the reference configuration corresponds to the one of the previous step. Definitely, all formulations give the same numerical results and the only advantage of using one rather than the others is the numerical effectiveness.

Moreover, on the one hand, a TL description is useful if rotations and displacements are large and strains are small (e.g. large strain hyperelastic rubber-like material). On the other hand, an UL description can be used advantageously in case of large plastic deformations. Accordingly, since the

deformation of the arch model is totally concentrated in the interface elements, exhibiting thus large displacements and strains, the UL has been selected. However, in order to evaluate possible inaccuracies, the analyses have been performed with and without implementing UL.

Regarding the stiffness of the interface elements, there is no doubt it plays the most important role. Since the peculiarity of the material adopted in the tests, in literature there are no indications for the stiffness parameters. Therefore, starting from the suggestion of Senthivel & Lourenço (2009), a sensitivity analysis has been performed. In particular the authors suggested for dry stack sawn masonry the values $K_n = 8$ N/mm^3 and $K_t = 3.3$ N/mm^3, respectively for normal and tangential stiffness (thus a ratio $K_t / K_n \cong 0.4$). In order to avoid large block interpenetration, values larger than $K_n = 0.1$ N/mm^3 and $K_t = 0.04$ N/mm^3 have been used.

Considering the horizontal displacement of the keystone as control point and a discretization of the interface by 32 elements, Figure 6 shows the capacity curve of the arch adopting three couples of interface stiffness, either with or without considering UL (dot and solid line, respectively). Neglecting UL, the curves approach asymptotically the result of the tilting test, showing, as expected, a steeper initial branch for stiffer interface. In case UL is accounted, instead, the results change dramatically. Although the early stage behavior is the same in both cases (with or without UL), the main difference is that the capacity never reaches the one provided by the tilting analysis, unless for large values of stiffness.

This behavior can be ascribed to the normal stiffness of the interface. A small value inevitably leads to interpenetration of the voussoirs and the position of the hinge (supposed either at the intrados or at the extrados) to move inward, "reducing" the effective thickness. This means the arch is basically thinner with a lower capacity. In reverse, a hypothetical infinite value would cause the hinges to locate on the edge line of the arch. In this regard, higher values of stiffness provide more suitable results.

Moreover, the softening branch of the curves clearly tends to a unique displacement (estimated equal to 6.6 mm) which can be regarded as the ultimate displacement of the arch. The envelope of all the curves can be approximated with the straight line reported in the figure. This shape parallels the nonlinear kinematic capacity curve of a rigid block undergoing horizontal forces and rocking in the base.

In the subsequent time history analysis, UL is considered, whereas the influence of the interface stiffness is estimated by means of a sensitivity analysis.

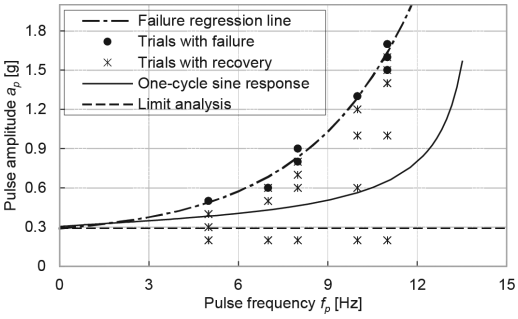

Figure 5. Results of the shaking table tests.

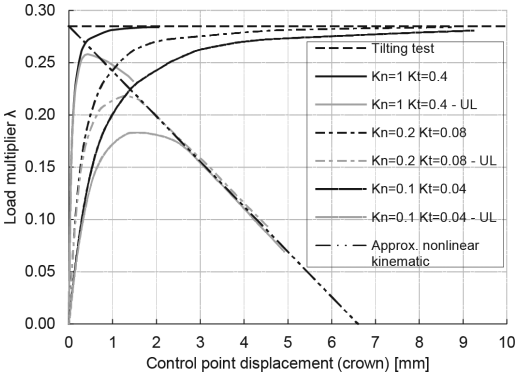

Figure 6. Arch capacity curves varying the interface stiffness.

4.2 *Time history analysis*

The accelerogram recorded on the slip table during the tests was used as input for the analysis. A minor filtering was necessary in order to correct the possible baseline drift and remove the higher frequencies content (low-pass filter). Moreover, the UL implementation requested a very small time step for the analysis to converge. In the present case, the time step was explicitly specified equal to 2×10^{-5} s.

Regarding the damping ratio, although several authors have proposed more or less sophisticated approach, sometimes simply fitting the numerical results to the experimental outcomes (Liberatore et al. 1997; Peña et al. 2006), this aspect still requests more research. The main difficulty is basically posed by the mathematical approximation of this phenomenon.

The most used approach is the viscous damping according to the Rayleigh formulation. However, two main drawbacks must be highlighted. Firstly, although for structures regarded as a continuum the damping ratio is usually set equal to 5%, for rigid block dynamics there is not clear recommendation. In case a DEM analysis is implemented,

the value adopted in literature is at least one order of magnitude smaller (De Lorenzis et al. 2007; Peña et al. 2006). Secondly, since the rigid block structures do not have natural frequencies (which depend on the overall displacement), it is not clear how to calculate the damping constants for the Rayleigh formulation.

Another possible schematization is represented by the structural damping, which is independent of the frequency and proportional to the displacement. It is usually suggested for models involving materials that exhibit frictional behavior or where local frictional effects are present throughout the model, such as dry rubbing of joints in a multi-link structure. Since the sliding occurrence was not evident in the tests and the present study is based on the stability of the arch (with large displacements), this form of damping can result in too conservative effects.

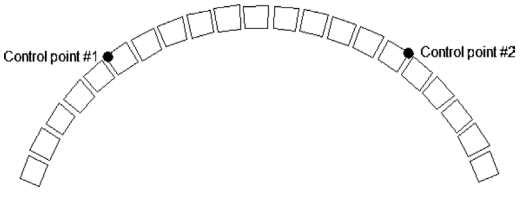

Figure 7. Sketch of the arch voussoirs by means of marker location and position of the control points.

According to the outcomes of the tests, few considerations must be done. Firstly, considering the impacts as the main source of energy dissipation, as described in §3.2 and Figure 4 only the hinges A and B were involved in small impacts (defined as migration) and a clear flipping movement was never recorded. Considering also the very small values proposed in literature for DEM analysis of dry-joint arches, in the present study, a null value of damping ratio was implemented.

With the aim of validating the model against the experimental results, as for the case of the push-over analysis, a sensitivity study regarding the interface stiffness was performed. This evaluation was essentially based on the comparison of the total displacement (in the plane of the arch) of two control points. In particular, the extrados corners of the sixth voussoir from both springs were selected as depicted in Figure 7. The position of Control point #2 is justified by the location of hinge C of Figure 4, whereas Control point #1 is simply the symmetric one with respect the central axis.

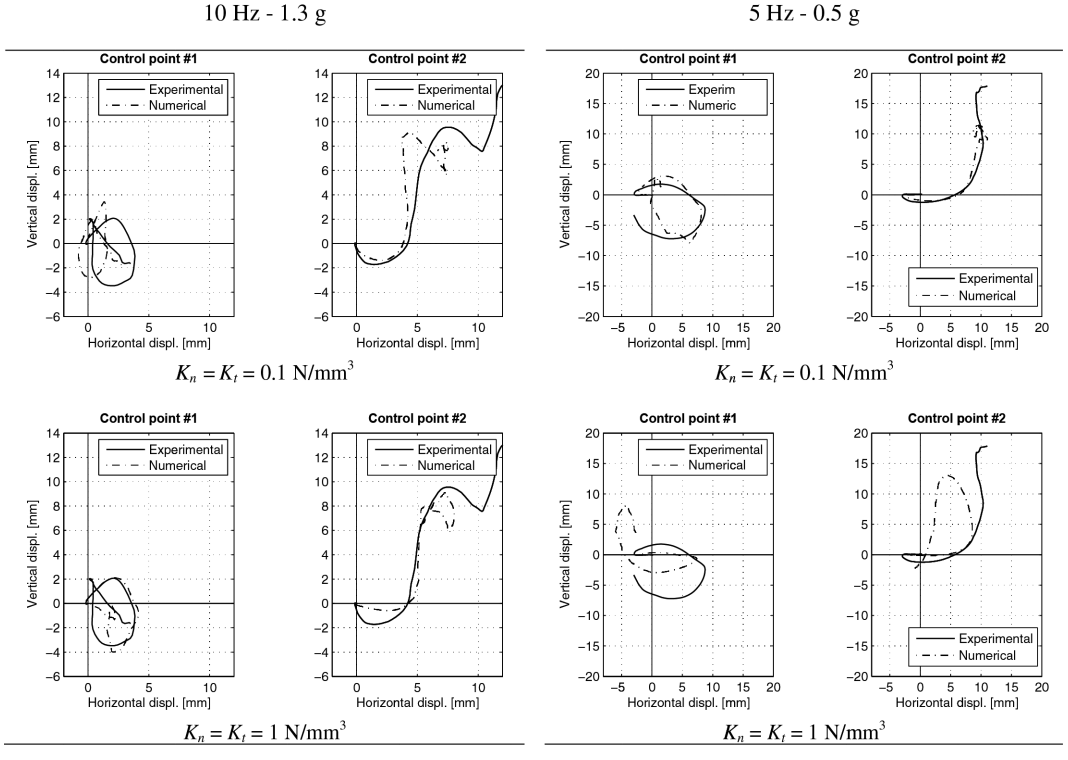

Figure 8. Displacement of the two control points: numerical and experimental results.

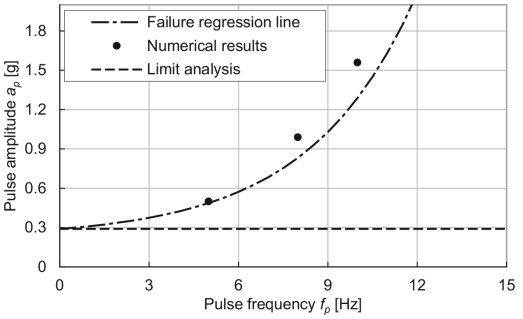

Figure 9. Results of the numerical analyses with $K_n = K_t = 0.1$ N/mm^3.

As far as the interface stiffness is concerned, K_n was considered equal to 0.01, 0.1, 1, 10, 100 N/mm^3, whereas K_t was assumed equal to 0.1, 0.4 and 1 time K_n, resulting thus 15 different sets. Whereas on the one hand the ratio 0.4 is the same proposed by Senthivel & Lourenço (2009), on the other hand, the ratio 0.1 and 1 were considered as limit values. Values of K_n out of the proposed range were also adopted, leading to severe problems of convergence.

This aspect is stressed also in literature. Although for DEM analysis the recommended values are much larger (order of magnitude of 10^{12} N/mm^3), De Lorenzis et al. (2007) stated that lower stiffness values led to contact overlap errors, whereas larger values led to excessively small time steps for the solution to remain stable.

Regarding the sensitivity analysis, for a given normal stiffness, the influence of the tangential stiffness was slightly notable. However, in case of large disparity between K_t and K_n, sliding between the blocks was evident, although not expected from both literature perspective (De Lorenzis et al. 2007; D'Ayala & Tomasoni 2011) and experimental evidences. Moreover, the best results were obtained considering $K_n = 0.1$, 1 N/mm^3.

For the sake of brevity, only the results of the analysis regarding $K_n = K_t = 0.1$, 1 N/mm^3 and the signals 10 Hz - 1.3 g and 5 Hz - 0.6 g are reported in Figure 8. In particular, the time history of the displacements of the control points is up to the end of the signals (0.3 and 0.6 s, respectively).

Finally, the results of the numerical analyses, considering the interface stiffness equal to $K_n = K_t = 0.1$ N/mm^3 are reported in Figure 9 (which parallels Figure 5). The numerical model matches well the experimental outcomes in the low frequency range, overestimating the capacity for higher frequency values. The collapse mechanisms are also well predicted by the numerical model.

5 CONCLUSIONS

In the present paper, the behavior of a dry-joint scaled arch undergoing windowed sine pulse was described. The experimental activity, monitored by a feature tracking technique, gave insights for the seismic behavior of the arch and provided valuable information to validate the FEM model. Great attention has been paid to the nonlinear properties of the friction interface elements, eventually proposing suitable values for both pushover and time history analysis.

The comparison with the results available in literature for one-cycle sine pulse (De Lorenzis et al. 2007; DeJong et al. 2008) highlighted two main outcomes. Firstly, considering the same amplitude and frequency, the windowed sine pulse resulted more conservative than the one-cycle sine pulse. This is due to the out-of-phase contribution of the former, which led to a more chaotic response. More research is still requested to understand the complex behavior of arched structures during an earthquake. In this regard, the windowed signals can be implemented to consider main pulses with initial conditions different from the rest position.

Secondly, the curve that better fits the failure cases is again of exponential type. Further experimental activities may extend this result to arches of different geometry and validate this trend for other kinds of pulse. This may represent an expedite and efficient tool for the seismic assessment of masonry arch in case a primary base acceleration impulse can be extracted from an earthquake motion.

Finally, the proposed simplified schematization about the hinge location could represent a valuable base for an analytical approach. In this regard, the available literature deals only with simple shape pulses with a symmetric behavior based on *a priori* defined mechanism. A more sophisticated model able to localize the hinges according to an energetic criterion is desirable.

REFERENCES

Clemente, P., 1998. Introduction to dynamics of stone arches. *Earthquake Engineering & Structural Dynamics*, 27(5): 513–522.

De Lorenzis, L., DeJong, M. & Ochsendorf, J., 2007. Failure of masonry arches under impulse base motion. *Earthquake Engineering & Structural Dynamics*, 36(14): 2119–2136.

DeJong, M. & Ochsendorf, J., 2006. Analysis of vaulted masonry structures subjected to horizontal ground motion. In P.B. Lourenco et al., eds. *5th International Conference on Structural Analysis of Historical Constructions*. New Delhi, India, 973–980.

DeJong, M. et al., 2008. Rocking Stability of Masonry Arches in Seismic Regions. *Earthquake Spectra*, 24(4): 847–865.

DeJong, M., 2009. *Seismic assessment strategies for masonry structures*. PhD dissertation, Massachusetts Institute of Technology.

D'Ayala, D. & Tomasoni, E., 2011. Three-dimensional analysis of masonry vaults using limit state analysis with finite friction. *International Journal of Architectural Heritage*, 5(2): 140–171.

Housner, G.W., 1963. The behavior of inverted pendulum structures during earthquakes. *Bulletin of the Seismological Society of America*, 53(2): 403–417.

Liberatore, D. & Spera, G., 2001. 'Response of slender blocks subjected to seismic motion of the base: Experimental results and numerical analyses. In T.G. Hughes & G.N. Pande, eds. *5th Int. Symposium on Computer Methods in Structural Masonry*. Rome, 117–124.

Liberatore, D., Larotonda, A. & Dolce, M., 1997. Analisi dinamica di archi in conci lapidei soggetti ad azioni sismiche. In *2nd Seminario Nazionale "Il patrimonio culturale e la questione sismica."* Rome, 551–571.

Moroni, M. & Cenedese, A., 2005. Comparison among feature tracking and more consolidated velocimetry image analysis techniques in a fully developed turbulent channel flow. *Measurement Science and Technology*, 16(11): 2307–2322.

Moroni, M. & Cenedese, A., 2015. Laboratory Simulations of Local Winds in the Atmospheric Boundary Layer via Image Analysis. *Advances in Meteorology*, 2015: 1–34.

Oppenheim, I.J., 1992. The masonry arch as a four-link mechanism under base motion. *Earthquake Engineering & Structural Dynamics*, 21(11): 1005–1017.

Peña, F., Lourenço, P.B. & Lemos, J.V., 2006. Modeling the dynamic behaviour of masonry walls as rigid blocks.

Senthivel, R. & Lourenço, P.B., 2009. Finite element modelling of deformation characteristics of historical stone masonry shear walls. *Engineering Structures*, 31(9): 1930–1943.

Shindler, L., Moroni, M. & Cenedese, A., 2012. Using optical flow equation for particle detection and velocity prediction in particle tracking. *Applied Mathematics and Computation*, 218(17): 8684–8694.

Zhang, J. & Makris, N., 2001. Rocking response of free-standing blocks under cycloidal pulses. *Journal of Engineering Mechanics*, 127(5): 473–483.